ELSEVIER

Chemical Physics 266 (2001) 251–271

Chemical Physics

www.elsevier.nl/locate/chemphys

Fifth-order electronically non-resonant Raman scattering: two-dimensional Fourier deconvolution

Laura J. Kaufman [a], Jiyoung Heo [a], Graham R. Fleming [a,*], Jaeyoung Sung [b,1], Minhaeng Cho [b]

[a] *Department of Chemistry, Physical Biosciences Division, Ernest Orlando Lawrence Berkeley National Laboratory, University of California, Berkeley, CA 94720, USA*

[b] *Department of Chemistry and Center for Multidimensional Spectroscopy, Korea University, Seoul 136-701, South Korea*

Received 25 October 2000

Abstract

This paper presents an analytical Fourier deconvolution procedure for homodyne detected electronically non-resonant fifth-order signal that reveals the bare nuclear response function free from the influence of the electronic (hyperpolarizability) responses generated by the five potentially overlapping finite duration pulses used in the experiment. In developing the fifth-order deconvolution procedure, an analogous procedure for homodyne detected third-order responses is elaborated. The potential implementation problems with the homodyne deconvolution procedure are evaluated through comparison of the third-order homodyne deconvolution result with that of the well-known third-order heterodyne deconvolution. Then, the homodyne deconvolution is extended to fifth-order where it is used on several measured tensor elements of the direct fifth-order signal. Suggestions are given for improving implementation of the procedure in fifth order so that more information on the direct fifth-order nuclear response as well as the hyperpolarizability responses can be recovered via the deconvolution procedure. © 2001 Elsevier Science B.V. All rights reserved.

Keywords: Raman scattering; Fourier deconvolution; Electronic responses

1. Introduction

Fifth-order electronically non-resonant Raman scattering is one of the new multi-dimensional spectroscopic techniques that offers information content unavailable in lower-order spectroscopies. In addition to its ability to separate homogeneous and inhomogeneous contributions to lineshapes [1], it is potentially also a sensitive probe of both interactions between and anharmonicities within nuclear motions as well as details of a system's potential surface [2–8].

In the experiment, two short laser pulses impinge upon the sample, leaving the system in a vibrational coherence. After a time delay, a second pair of ultrafast pulses transfers the system to a second coherence state or to a population state. After a second time delay, a final short pulse

* Corresponding author. Tel.: +1-510-643-7609; fax: +1-510-642-6340.

E-mail address: GRFleming@161.gov (G.R. Fleming).

[1] Present address: Department of Chemistry, Massachusetts Institute of Technology, Cambridge, MA 02139, USA.

0301-0104/01/$ - see front matter © 2001 Elsevier Science B.V. All rights reserved.
PII: S0301-0104(01)00251-8

stimulates a Raman scattering event in a particular phase-matched direction. The two variable time delays in the experiment, τ_2 and τ_4 in our notation, are the two time dimensions in this spectroscopy, and a full two-dimensional signal is collected, with approximately equal time steps across each dimension.

While the one-dimensional spectroscopies analogous to two-dimensional Raman scattering, most notably the time-resolved four wave mixing technique OHD-OKE, contributed and continue to contribute valuable information to the understanding of condensed phase dynamics, especially in terms of the intermolecular dynamics of liquids, these experiments are inherently more limited than the two-dimensional measurement. Where the electronically non-resonant one-dimensional four wave mixing experiments mentioned probe the ensemble average of correlations between polarizability operators at two different times, the two-dimensional experiment probes correlations between polarizability operators at three different times before the quantity is ensemble averaged. Taking the ensemble average after a three-point, two-time correlation function as opposed to after a two-point, one-time correlation function, peels back one layer of the ensemble averaging that necessarily occurs in experiments exciting and probing a collection of molecules. Despite this limitation on one-dimensional measurements, by varying external parameters, fitting the measured spectra, and collecting real and imaginary contributions to the signal separately, valuable information about the types and timescales of intermolecular motions has been obtained as have descriptions of relative homogeneities of liquids. However, due at least partly to the nature of the ensemble taken, these one-dimensional signals are generally broad and fairly featureless. These broadenings make it difficult to use these techniques to learn microscopic details of the intermolecular motions of liquids, so important to all solvation processes. In contrast, when the information is ensemble averaged after a second time delay and is spread out over two time dimensions, microscopic details of such dynamics become more apparent. So, in the same way that multi-dimensional NMR allows access to structural information unavailable in one-dimensional techniques, two-dimensional time-domain spectroscopies allow access to structural and dynamical information formally buried in one-dimensional signals.

Despite the great promise two-dimensional fifth-order Raman spectroscopy holds for elucidating detailed behavior of condensed phase systems [1–6,8–17], experimentally it has proven difficult, and the potential for the technique clearly has not yet been fully realized. However, we believe the greatest technical difficulty affecting two-dimensional Raman spectroscopy (the potential for third-order cascade signals to dominate the desired direct fifth-order signal) has now been recognized [18–20] and overcome by several groups [18,21–23], and the fifth-order, two-dimensional non-resonant Raman technique has now been used to study the intermolecular motions of CS_2. While the successful applications of the two-dimensional fifth-order Raman technique have provided evidence for the dephasing timescale of room temperature CS_2, details of the microscopic dynamics in terms of contributions from librational type motion, collision-induced terms, and reorientational dynamics have been more difficult to attain from the measured spectra. Such details are difficult to ascertain from the experiments performed to date based on both collection methods and limited theoretical development. The only experiments to date that explore the full polarization selectivity of the signal were collected with homodyne detection [21,24]. As such, knowledge of the absolute sign and phase of the response functions is unavailable (and can not be recovered with the deconvolution procedure that will be presented here). Further, because only one theory that explicitly accounts for the polarization dependence of the fifth-order signal is available [10,11], extraction of detailed information from these polarization dependent experiments is difficult. Heterodyne detected experiments hold the promise of measuring the sign, phase, and polarization dependence of the fifth-order signal. However, heterodyne detected measurements have thus far been experimentally limited to collecting only one tensor element of the fifth-order signal [22,23]. This group is currently working on setting up a heterodyne detected experiment that can

probe all of the tensor elements of the fifth-order response. This experimental advance along with continued theoretical effort in terms of polarization dependence of the signal will mitigate the difficulties in extracting the interesting information regarding detailed dynamics from the fifth-order experiment.

Even though measurements of the polarization selected heterodyne detected direct fifth-order signal will contain the information regarding the nature and magnitude of couplings between different motions, the signal does not contain this information alone: instead, because finite duration pulses are used, it contains a convolution of the response function and the pulse profiles. In third-order heterodyne detected OHD-OKE experiments a Fourier deconvolution procedure has been performed to remove the effects arising from the use of finite duration pulses and to reveal the bare nuclear response function. The benefits of such a procedure in third-order extend directly to fifth-order. The deconvolution procedure affords direct observation of the nuclear response function alone by confining the instantaneous electronic (or hyperpolarizability) responses to time zero for third-order experiments and to the two time axes for fifth-order experiments. Further, Fourier deconvolution removes spectral filtering effects caused by finite pulses so that high frequency motions are not artificially damped due to the pulse duration [25]. Another benefit of such a procedure is that data collected with different pulse profiles will be directly comparable. All of these benefits hold for both the one-dimensional and the two-dimensional experiments, though in the two-dimensional experiment they may be even more important because finite duration pulses convolute with the desired pure nuclear response function across two time variables in these experiments. Thus, the information not only around the time origin but also along the two time axes is compromised by the involvement of the finite duration pulses. The $\tau_2 = 0$ fs and $\tau_4 = 0$ fs axes contain information regarding the hyperpolarizability (electronic) responses not accessible in lower-order experiments, and the $\tau_2 = 0$ fs axis can also include information on population dynamics [15,21]. It would be valuable to clearly separate the hyperpolarizability responses from the nuclear response present in the true two-dimensional area since in the absence of cascade signals that signal must be due to fifth-order three-point polarizability correlation functions. For these reasons, we have developed a two-dimensional Fourier deconvolution for the fifth-order non-resonant Raman response.

2. Theory

The homodyne detected direct fifth-order signal S can be expressed as

$$S \propto \int_{-\infty}^{\infty} \mathrm{d}t\, \overline{\varepsilon(t) \cdot \varepsilon(t)} \propto \int_{-\infty}^{\infty} \mathrm{d}t\, \overline{\mathbf{P}^{(5)}(t) \cdot \mathbf{P}^{(5)}(t)}, \quad (1)$$

where $\varepsilon(t)$ denotes the vector of the electric field whose source is the oscillating matter-polarization vector $\mathbf{P}^{(5)}$ induced by the fifth-order interaction between the system and the five external electric fields. Here, $\overline{X}$ denotes the cycle-averaged value of an oscillating quantity X. As described in the introduction, in the fifth-order Raman scattering experiment, synchronized pairs of electric fields impinge upon the system at time 0 and at time τ_2, before the probe pulse impinges at a later time, $\tau_2 + \tau_4$. Thus, the external electric field vector is given by a sum of the five fields,

$$\mathbf{E}_{\mathrm{ex}}(\mathbf{r}, t) = \sum_{j=1}^{5} \hat{\mathbf{e}}_j E_j(t) \exp(\mathrm{i}\mathbf{k}_j \cdot \mathbf{r} - \mathrm{i}\omega_j t) + \mathrm{c.c.} \quad (2)$$

with the temporal envelope function $E_j(t)$ given by

$$\begin{aligned} E_1(t)/E_1^0 &= E_2(t)/E_2^0 \\ &= (\pi\alpha)^{-1/4} \exp(-t^2/2\alpha) \\ &\equiv \phi_1(t), \\ E_3(t)/E_3^0 &= E_4(t)/E_4^0 \\ &= (\pi\alpha)^{-1/4} \exp[-(t-\tau_2)^2/2\alpha] \equiv \phi_3(t), \\ E_5(t)/E_5^0 &= (\pi\alpha)^{-1/4} \exp[-(t-\tau_2-\tau_4)^2/2\alpha] \\ &\equiv \phi_5(t). \end{aligned} \quad (3)$$

In Eq. (2), $\hat{\mathbf{e}}_j$ denotes the unit vector whose direction is parallel to the jth input electric field vector, and in Eq. (3), E_j^0 denotes the maximum value of the magnitude of the jth electric field

vector, and α is related to the full-width-half-maximum (FWHM) of the pulse intensity by $\alpha = (\mathrm{FWHM})^2/4\ln 2$. The non-linear polarization vector $\mathbf{P}^{(5)}$ is related to the input electric field vector as follows:

$$\mathbf{P}^{(5)}(\mathbf{r},t) = \int_0^\infty \mathrm{d}s_2 \times \int_0^\infty \mathrm{d}s_1 \overleftrightarrow{\mathbf{R}}(s_1,s_2)\cdots \mathbf{E}_{\mathrm{ex}}(t)\mathbf{E}_{\mathrm{ex}}^2(t-s_2) \times \mathbf{E}_{\mathrm{ex}}^2(t-s_2-s_1). \tag{4}$$

Here, s_1 and s_2 are the times between the first and second field–matter interactions and second and third field–matter interactions, respectively, and are thus the time arguments of $\overleftrightarrow{\mathbf{R}}(s_1,s_2)$, a sixth-rank tensor quantity. $\overleftrightarrow{\mathbf{R}}(s_1,s_2)$ is a non-linear response function that describes the response of the system polarization due to the five time perturbations of the external field vectors. The polarization vector given in Eq. (4) is the sum of various component vectors, each of which propagates in a specific direction and corresponds to an optical process occurring in the system. Mathematically, $\overleftrightarrow{\mathbf{R}}(s_1,s_2)$ corresponds to one of various combinations of the wave vectors of the input electric-field components in Eq. (3). In an experiment, one can measure the contribution from a specific component $\mathbf{P}_S^{(5)}$ of the polarization vector by observing the output radiation in a specific propagating direction: this enables one to observe a specific optical process exclusively. From now on, we will consider this situation, and we will denote the wave vector and frequency of the output radiation as $\mathbf{k}_S$ and ω_S, respectively.

Now, we write $\mathbf{P}_S^{(5)}$ as

$$\mathbf{P}_S^{(5)}(\mathbf{r},t) = \int_0^\infty \mathrm{d}s_2 \int_0^\infty \mathrm{d}s_1 \mathbf{R}(s_1,s_2) \times \left(\prod_{j=1}^{5} E_j^0\right)\phi_5(t)\phi_3^2(t-s_2) \times \phi_1^2(t-s_2-s_1)\exp(\mathrm{i}\mathbf{k}_S\cdot\mathbf{r} - \mathrm{i}\omega_S t). \tag{5}$$

Here, $\mathbf{R}(s_1,s_2)$ denotes the response function vector defined by the contraction of the sixth rank response function tensor $\overleftrightarrow{\mathbf{R}}(s_1,s_2)$ with the unit vectors $\hat{\mathbf{e}}_j$ of the five external electric fields, i.e., $\mathbf{R} = \overleftrightarrow{\mathbf{R}}\cdots\hat{\mathbf{e}}_5\hat{\mathbf{e}}_4\hat{\mathbf{e}}_3\hat{\mathbf{e}}_2\hat{\mathbf{e}}_1$. Therefore, $\mathbf{R}$ depends on the polarization direction of the five input electric field vectors. From Eqs. (1) and (5) we can obtain the expression of the signal as,

$$S \propto \int_{-\infty}^{\infty} \mathrm{d}t\,\phi_5^2(t)\left|\int_0^\infty \mathrm{d}s_2 \int_0^\infty \mathrm{d}s_1\,\mathbf{R}(s_1,s_2)\phi_3^2(t-s_2) \times \phi_1^2(t-s_2-s_1)\right|^2, \tag{6}$$

where the modulus operation $|\mathbf{V}|$ denotes the magnitude of a vector quantity $\mathbf{V}$. Because $\mathbf{R}$ is parallel to $\mathbf{P}_S^{(5)}$, we can write $\mathbf{R}(s_1,s_2) = R(s_1,s_2)\hat{\mathbf{p}}$ with $\hat{\mathbf{p}} = \mathbf{P}_S^{(5)}/|\mathbf{P}_S^{(5)}|$. Therefore, Eq. (6) can be written in terms of scalar quantities as follows:

$$S \propto \int_{-\infty}^{\infty} \mathrm{d}t\,\phi_5^2(t)\left[\int_0^\infty \mathrm{d}s_2 \int_0^\infty \mathrm{d}s_1 R(s_1,s_2)\phi_3^2(t-s_2) \times \phi_1^2(t-s_2-s_1)\right]^2. \tag{7}$$

Note that in the limit of $\alpha \to 0$, the scaled envelope function $\phi_j(t)$ defined in Eq. (3) becomes $\phi_1^2(t) \to \delta(t)$, $\phi_3^2(t) \to \delta(t-\tau_2)$, and $\phi_5^2(t) \to \delta(t-\tau_2-\tau_4)$, with $\delta(t)$ being Dirac delta function, and hence Eq. (7) becomes $S \propto [R(\tau_2,\tau_4)]^2$. This corresponds to the situation where the timescale of the pulse envelope change is negligibly small compared with that of the response function evolution.

For finite pulse width, denoting a Gaussian function as $g(t) = (\pi\alpha)^{-1/2}\exp(-t^2/\alpha)$, we can rewrite Eq. (7) as

$$S(\tau_2,\tau_4) \propto \int_{-\infty}^{\infty} \mathrm{d}t\, g(t-\tau_2-\tau_4) \times \left[\int_0^\infty \mathrm{d}s_2 \int_0^\infty \mathrm{d}s_1\, R(s_1,s_2) \times g(t-\tau_2-s_2)g(t-s_2-s_1)\right]^2. \tag{8}$$

Although Eqs. (3) and (8) assume the shape of the scaled pulse envelope function is given by a Gaussian, this is not required, and the procedure is equally applicable to other types of envelope

functions. By changing the integration variable, $t' = t - \tau_2$, Eq. (8) reads

$$S(\tau_2,\tau_4) \propto \int_{-\infty}^{\infty} \mathrm{d}t' g(t'-\tau_4) \times \left[\int_0^{\infty} \mathrm{d}s_2 \int_0^{\infty} \mathrm{d}s_1 R(s_1,s_2) \times g(t'-s_2) g(t'+\tau_2-s_2-s_1) \right]^2. \tag{9}$$

Denoting the double integral in the square bracket on the right side of Eq. (9) as $f(t',\tau_2)$, one can see that for fixed τ_2 the expression for $S(\tau_2,\tau_4)$ is a convolution integral over t'. Thus we have

$$S(\omega_4,\tau_2) \equiv \int_{-\infty}^{\infty} \mathrm{d}\tau_4 \, \mathrm{e}^{\mathrm{i}\omega_4\tau_4} S(\tau_2,\tau_4) \propto \tilde{g}(\omega_4)\tilde{f}(\omega_4,\tau_2), \tag{10}$$

where $\tilde{X}(\omega) \equiv \int_{-\infty}^{\infty} \mathrm{d}t \, \mathrm{e}^{\mathrm{i}\omega t} X(t)$. Therefore, by dividing the Fourier transform of the measured signal data, $S(\omega_4,\tau_2)$, by the Fourier transform of the pulse intensity profile, $\tilde{g}(\omega_4)$, we can obtain the Fourier transform of the double integral in the square bracket on the right-hand side of Eq. (9), i.e., $\tilde{f}(\omega_4,\tau_2) \propto S(\omega_4,\tau_2)/\tilde{g}(\omega_4)$. Then, the inverse Fourier transform of $\tilde{f}(\omega_4,\tau_2)$ over ω_4 results in

$$f(u,\tau_2) \equiv \frac{1}{2\pi} \int_{-\infty}^{\infty} \mathrm{d}\omega_4 \, \mathrm{e}^{-\mathrm{i}\omega_4 u} \tilde{f}(\omega_4,\tau_2) = \left[\int_0^{\infty} \mathrm{d}s_2 \int_0^{\infty} \mathrm{d}s_1 R(s_1,s_2) g(u+\tau_2-s_2 - s_1) g(u-s_2) \right]^2. \tag{11}$$

By introducing $R_{\mathrm{F}}(s_1,s_2) = R(s_1,s_2)\Theta(s_1)\Theta(s_2)$ with $\Theta(s)$ being a heavyside step function, we can rewrite Eq. (11) as

$$f^{1/2}(u,\tau_2) \equiv \Sigma(u,\tau_2) = \int_{-\infty}^{\infty} \mathrm{d}s_2 \int_{-\infty}^{\infty} \mathrm{d}s_1 R_{\mathrm{F}}(s_1,s_2) \times g(u+\tau_2-s_2-s_1) g(u-s_2). \tag{12}$$

It should be noted that the introduction of R_{F} here is made only for mathematical efficacy. Because the response function describes the response of matter resulting from the perturbation, according to the causality principle the response vanishes before the perturbation is applied. Mathematically terms, this means $R(s_1,s_2) = 0$ when either s_1 or s_2 becomes negative, so that $R_{\mathrm{F}} = R$.

Making the following substitutions:

$$u + \tau_2 = v, \quad s_1 + s_2 = \xi, \quad s_2 = \zeta,$$
$$\Sigma(u,\tau_2) = \Sigma'(u,v),$$

and

$$R(s_1,s_2) = R'(\xi,\zeta),$$

Eq. (12) reads,

$$\Sigma'(u,v) = \int_{-\infty}^{\infty} \mathrm{d}\zeta \int_{-\infty}^{\infty} \mathrm{d}\xi R'(\xi,\zeta) g(v-\xi) g(u-\zeta) = \int_{-\infty}^{\infty} \mathrm{d}\zeta R''(\zeta,v) g(u-\zeta), \tag{13}$$

where $R''(\zeta,v) = \int_{-\infty}^{\infty} \mathrm{d}\xi R'(\xi,\zeta) g(v-\xi)$. Again, for fixed v, the second equality of Eq. (13) is another convolution integral, so we obtain

$$\tilde{\Sigma}'(\omega_4,v) = \int_{-\infty}^{\infty} \mathrm{d}u \, \Sigma'(u,v) \mathrm{e}^{\mathrm{i}\omega_4 u} = \tilde{R}''(v,\omega_4)\tilde{g}(\omega_4). \tag{14}$$

Eq. (14) allows us to find $\tilde{R}''(v,\omega_4)$ from the Fourier transform, $\tilde{\Sigma}'(\omega_4,v)$, of $\Sigma'(u,v)$, which was obtained earlier from Eq. (12). As previously, by performing the inverse transformation on $\tilde{R}''(v,\omega_4)$ over ω_4, we get the time domain expression for $\tilde{R}''$:

$$R''(v,\zeta) = \frac{1}{2\pi} \int_{-\infty}^{\infty} \mathrm{d}\omega_4 \, \mathrm{e}^{-\mathrm{i}\zeta\omega_4} \tilde{R}''(v,\omega_4) = \int_{-\infty}^{\infty} \mathrm{d}\xi R'(\xi,\zeta) g(v-\xi). \tag{15}$$

Again, one can see that Eq. (15) has the form of a convolution integral (for ξ), so we get

$$\tilde{R}''(\omega_2,\zeta) = \int_{-\infty}^{\infty} \mathrm{d}v \, \mathrm{e}^{\mathrm{i}\omega_2 v} R''(v,\zeta) = \tilde{R}'(\omega_2,\zeta)\tilde{g}(\omega_2) \tag{16}$$

and $\tilde{R}'(\omega_2,\zeta) = \tilde{R}''(\omega_2,\zeta)/\tilde{g}(\omega_2)$. By performing an inverse transform on the obtained $\tilde{R}'(\omega_2,\zeta)$, we finally recover the bare response function:

$$R'(\xi,\zeta) = \frac{1}{2\pi}\int_{-\infty}^{\infty} \mathrm{d}\omega_2\, \mathrm{e}^{-\mathrm{i}\xi\omega_2}\tilde{R}'(\omega_2,\zeta) = R(s_1,s_2). \quad (17)$$

In summary, despite the many changes of variables presented in the theoretical development of the two-dimensional deconvolution procedure, the procedure is straightforwardly applied to the raw data by employing three Fourier transforms, divisions by the Fourier transformed pulse profile, and inverse Fourier transforms. The first two Fourier transforms are performed along the τ_4 axis, while the third is performed along the τ_2 axis.

3. Experimental

As discussed in detail elsewhere, a standard titanium sapphire oscillator was used to generate 1 nJ, 28 fs ((pulse intensity) Gaussian, FWHM) pulses centered at 800 nm [26]. The pulses were regeneratively amplified resulting in 25 μJ/pulse, 42 fs, 800 nm pulses at a repetition rate of 1.5 kHz [27]. The regenerative amplifier was pumped by a Q-switched, diode-pumped Nd:YLF laser (Light-Wave Electronics) with shot-to-shot root-mean-squared intensity fluctuations of <0.5% at 532 nm resulting in very small power fluctuations at our sample. Following attenuation to approximately 10 μJ/pulse, the pulse was split into five pulses of nearly equal intensity, ~2 μJ per pulse per beam. Pulse duration was determined by off-axis autocorrelation measurements in a 150 μm BBO crystal. Mechanical translation stages with stepping resolution of 0.1 μm (Newport) were used to sweep the two adjustable time variables, τ_2 and τ_4, in such a way as to collect surfaces as a function of the two time delays between the pairs of laser pulses directly [18]. The polarization of each beam was individually adjusted by a $\lambda/2$ waveplate. In the measurement of the direct fifth-order signal a 28.9 cm focal length singlet lens was used to focus the five beams into a 1.0 mm sample cell containing CS_2 at room temperature. The fifth-order signal emerged in a well-defined phase-matched direction, and irises were used to spatially select the signal, which was filtered through an 800 ± 20 nm filter and detected using an IR extended photomultiplier tube (Hamamatsu, R636-10). To assist in spatial location of the signal, a sixth beam aligned along the signal direction was used to arrange the detection setup and was blocked before data collection began. Neither the aligning beam nor the photo-multiplier tube was used in the collection of the more intense cascade and third-order signals that will be presented in this paper, yet irises were used to spatially select and aperture those signals. One of the five incoming beams was mechanically chopped at half the laser repetition rate, and the signal was collected by a lock-in amplifier synchronized to the mechanical chopping frequency.

In other publications, details of the current phase-matching geometry [21,24] and details of the current phase-matching calculations [21] were presented. Here, a summary is given. It has been shown that early measurements of the fifth-order signal were dominated by third-order cascade processes and carried no more information than ordinary third-order measurements [18–20,28]. Such an error was possible because both the direct and cascade fifth-order signals emerge in the same phase-matched direction, $k_S = (k_1 - k_2) - (k_3 - k_4) + k_5$, and both are fifth-order in their power dependence on the incoming beam intensity. There are two types of cascade signals (symmetric and parallel), and many of the early phase-matching geometries were designed expressly to avoid contamination by symmetric cascades. However, parallel cascades were not considered, and thus early results were dominated by parallel cascades. These cascades are comprised of third-order responses and are governed by the following equation:

$$R^{(3)^2}_{nmlkji,\mathrm{parallel}} = R^{(5)}_{\mathrm{par}}(\tau_2,\tau_4) = R^{(3)}_{\Sigma mji}(\tau_2+\tau_4)R^{(3)}_{n\Sigma lk}(\tau_4) + R^{(3)}_{\Sigma mlk}(\tau_4)R^{(3)}_{n\Sigma ji}(\tau_2+\tau_4). \quad (18)$$

The subscripts here refer to the polarizations of the incoming beams and read from right to left with

the leftmost subscript referring to the polarization of the signal field.

By taking advantage of the fact that all the cascade processes have an intermediate step, in which a signal emerges that acts as either the pump (symmetric cascades) or probe (parallel cascades) for a second third-order event, a geometry that suppresses cascades can be designed. A geometry for the incoming beams in which *all* cascade processes are very poorly phase matched, while the overall direct fifth-order process remains well phase matched, has been used to collect all direct fifth-order signals presented in this paper [24]. Using this geometry, measurements have now been made for many tensor elements of the direct fifth-order signal, and these measurements are only very minimally contaminated by third-order cascades [21]. Other techniques, taking advantage of the 90° difference in phase between the direct fifth-order signal and cascade signal, (assuming perfect phase matching of all signals) have also been used to collect direct fifth-order signal [22,23]. In this paper, the deconvolution procedure presented is for a signal that includes only the direct fifth-order signal. The presence of a very small amount of cascade signal in the data on which the deconvolution will be performed is not expected to have a large effect on the resulting spectra. The deconvolution procedure presented in Section 2 of this paper could also be used on a cascade signal. The procedure would be the same, but the result would be the bare response functions of the cascade signal as presented in Eq. (18), not the direct fifth-order response function.

In addition to the direct fifth-order and cascade signals that will be presented and deconvoluted in this paper, heterodyne detected third-order data collected in a pump–probe geometry are presented, as are homodyne detected four wave mixing third-order data collected in a box geometry. The heterodyne detected third-order data will be used to demonstrate the one-dimensional Fourier deconvolution that has been used previously for third-order OHD-OKE measurements. The homodyne detected third-order data will be used to present a one-dimensional analogue to the two-dimensional Fourier deconvolution for which the theory is presented above.

4. Results and discussion

4.1. Implementation

Certain approximations must be made in implementing the procedure. One area that may require approximations in order to perform the two-dimensional Fourier deconvolution is that of pulse shape and width. For our homodyne deconvolutions, we have assumed a Gaussian pulse with an intensity FWHM of ~50 fs for the fifth-order measurements and one with a FWHM of ~60 fs for the third-order measurement. We deduce these shapes and widths from autocorrelation measurements taken for the pulse after it is split into three or five beams. These autocorrelation functions are all well fit by Gaussians with FWHMs of ~70 and 84 fs, respectively. The assumption of a shape and width for the pulse intensity is unnecessary in the deconvolution of a heterodyne detected third-order experiment as was shown by McMorrow et al. [25,29,30] and as will be reviewed here. Because the commonly measured autocorrelation function, as opposed to the electric field alone, appears in the deconvolution integral, this commonly measured function can be inserted directly into the deconvolution formula. We have attempted to assess the importance of pulse shape in the deconvolutions in two ways. First, we have performed the third-order heterodyne deconvolution with the actual autocorrelation function and with a pulse profile assumed to be Gaussian. This will help assess the importance of assuming a pulse shape instead of using a known function, as we must do in the homodyne deconvolutions. Fig. 1 shows an example of an autocorrelation measurement and its fit to a Gaussian. While it fits well at higher intensities, the wings of the measured autocorrelation are clearly broader than those of either a Gaussian or a sech^2 pulse. The results of this comparison will be discussed in Section 4.2. Second, we have performed third- and fifth-order homodyne deconvolutions, where measured autocorrelation functions can not be used, with both Gaussian and sech^2 pulse intensity profile assumptions. Since the actual pulse shape is suspected to have a small amplitude slowly decaying feature (as deduced from the autocorrelation

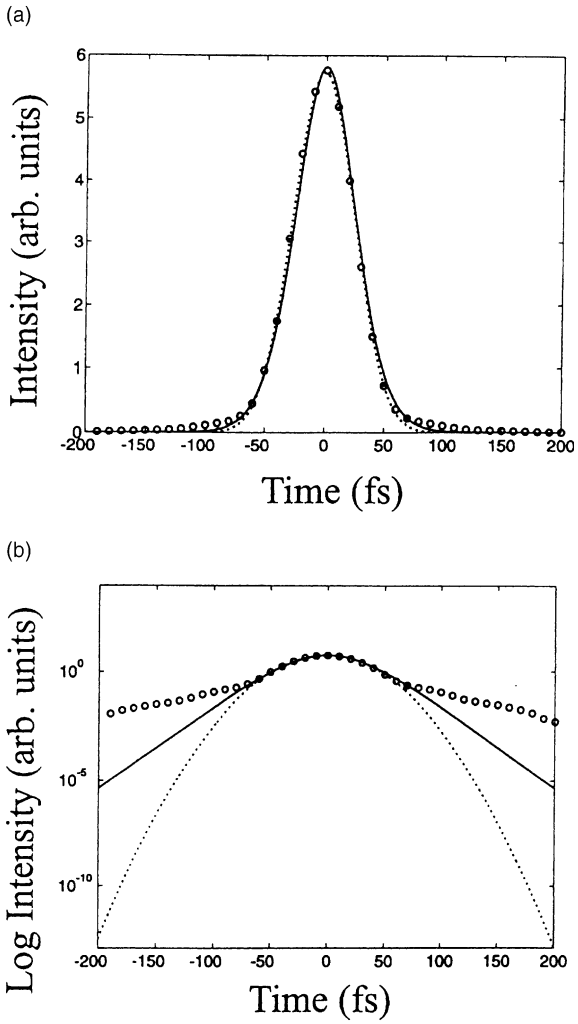

Fig. 1. (a) Measured autocorrelation function of pulse used in the heterodyne detected measurement presented in this paper. The data (-○-) is well fit by both a Gaussian (···) of intensity FWHM 43 fs and a sech^2 (—) of intensity FWHM 39 fs. (b) Same autocorrelation and fits on a log intensity vs. time plot.

measurement presented in Fig. 1), the deconvolution assuming a Gaussian pulse can not completely remove the pulse and could affect the early time results. The sech^2 pulse is chosen to test the deconvolution because its corresponding autocorrelation function fits the measured autocorrelation of our pulse at longer times better than does a Gaussian (Fig. 1). Thus using a sech^2 pulse compared to using a Gaussian pulse can test the effect of a long time tail in the homodyne deconvolution. Again, this is not necessary in the heterodyne deconvolution where the autocorrelation function is included directly. As shown in Fig. 1, a typical pulse used in our third-order heterodyne detected measurements was best fit by a 43 fs Gaussian or a 39 fs sech^2 ($I(t)$). The log plot, however, shows that the two functions are significantly different in their time tails and that neither follows the shape of the measured autocorrelation function. The deconvolutions using these pulses will be briefly discussed in Section 4.2.

The third-order measurements we will use in the heterodyne deconvolution were collected in a pump–probe geometry and, unlike the later OHD-OKE experiments of McMorrow et al. [31–33] were not phase selected in the detection. This will be discussed further below. In addition, while the OHD-OKE experiment measures the anisotropic R_{zzzz}–R_{zyzy} component of the response [34,35] (which equivalently measures the R_{zzzz}–R_{yyzz} component when considering only nuclear dynamics) [36,37], we measure these responses separately and deconvolute the R_{zzzz} response.

So, in the case of heterodyne detected third-order signal, the measured signal can be expressed as

$$S(\tau) = \int_{-\infty}^{\infty} \mathrm{d}t \sum_{l,k} E^*_{\mathrm{LO}}(\omega_l, t-\tau) E_k(\omega_k, t-\tau) \times \int_{-\infty}^{t} \mathrm{d}t' R_{lkji}(t-t') \sum_{j,i} E^*_j(\omega_j, t') E_i(\omega_i, t'). \tag{19}$$

In the case of a pump, probe, and local oscillator derived from a single transform-limited pulse, this can be expressed as

$$S(\tau) = \int_{-\infty}^{\infty} \mathrm{d}t\, G^{(2)}(\tau - t) R_{lkji}(t), \tag{20}$$

where $G^{(2)}(t)$ is the intensity autocorrelation function of the pulse [25,34]. This is a convolution integral over t, so that a division of the Fourier-transformed (FT) signal by the FT autocorrelation function leaves $R(\omega)$, the bare frequency domain response function. An inverse transform then allows one to obtain $R(t)$, the time-domain response

function. This deconvolution procedure has proven facile to employ and effective on data with reasonable signal to noise.

On the other hand, the homodyne detected signal measures

$$S(\tau) = \int_{-\infty}^{\infty} \mathrm{d}t \left| \sum_k E_k(\omega_k, t-\tau) \int_{-\infty}^{t} \mathrm{d}t' R_{lkji}(t-t') \times \sum_{j,i} E_j^*(\omega_j, t') E_i(\omega_i, t') \right|^2 . \quad (21)$$

No similar simplification of the measured signal is possible, and thus we would generally require precise knowledge of the laser pulse amplitude profile to deconvolute the signal [25]. If, however, a delta function probe pulse is assumed, the problem reduces to that of the heterodyne detected signal. We wish to avoid such an approximation, and we do so by employing a deconvolution procedure for the homodyne detected third-order measurement that is analogous to that presented in Section 2 of this paper for the fifth-order homodyne detected signal. Unlike the heterodyne deconvolution, this deconvolution requires two Fourier transforms and inverse Fourier transforms to obtain the bare response function, making the result more susceptible to numerical errors than the heterodyne detected third-order signal.

Another issue that must be addressed is the reality of the homodyne detected signal to be deconvoluted. As has been mentioned previously, the OHD-OKE technique allows for separate collection of the real (dichroic) and imaginary (birefringent) portions of the signal, and several experiments have phase selected the signal to measure these contributions separately [30–33,38,39]. We do not measure these contributions separately with our heterodyne technique, but we do predominantly measure birefringence with both our heterodyne [37,40–42] and homodyne techniques. Also, the third- and fifth-order homodyne deconvolutions require that a square root be taken. In doing so, we assume that the response function is entirely real. We believe this to be an acceptable approximation in the case of CS_2, where electronically non-resonant processes dominate and any dichroic response is very small in comparison [34] as has been shown for the R_{zzzz} tensor element CS_2 [38,39]. As expected, around the time origin, where three pulses overlap, the proportion of the signal due to dichroism is greater, and may contribute up to 12% of the homodyne detected signal [39]. While in general the shape of the very small dichroic portion of the response of CS_2 resembles that of the birefringent portion [37] it should be noted that heterodyne experiments show that part of the imaginary portion of $R_{zzzz}(t)$ is negative, so it is not obvious how a signal containing both the real and imaginary portions of the response will look. Thus the use of the square root function in the homodyne deconvolutions is not exact, nor is the comparison with the OHD-OKE phase-selected measurements. In the fifth-order experiment, the reality of the response remains a bigger question than in third-order because when many pulses are overlapped resonant absorption (imaginary) responses may be more important. In the fifth-order experiment, five pulses are overlapped at the origin and four pulses are overlapped along the two axes. It is not yet known how large the imaginary part of the fifth-order signal is. However, the results of third-order phase selected measurements show that the polarizability responses of CS_2 are dominated by birefringence, and we assume that this is true of the fifth-order polarizability responses as well.

The final implementation difficulties relate to data collection constraints and numerical limitations of Fourier transforms. First, oscillations in Fourier transformed signals can be related to the Nyquist critical frequency. For discretely sampled data the Nyquist critical frequency is given by $f = 1/2\Delta$ with Δ the time interval between consecutive data, and the Fourier transform is only defined from the negative to positive values of the Nyquist critical frequency. At frequencies approaching the Nyquist critical frequency, oscillations in Fourier-transformed data increase dramatically. The time spacing used in collecting the third-order signals presented varied from ~5 fs at short times to 20 fs at the longest times collected (several picoseconds). The third-order data sets were splined so that all the steps were equivalent to the smallest time step taken, generally 3–5 fs. This splining has been shown to be acceptable

previously, and these time steps satisfy the Nyquist criterion that demands that $1/c\Delta t \geqslant \Delta\omega$ with Δt the sampling frequency and $\Delta\omega$ the bandwidth of the experiment [32]. For this experiment with 40–50 fs pulses, $\Delta\omega$ is $\leqslant 700$ cm^{-1} and $1/c\Delta T$ is $\geqslant 3000$ cm^{-1}, so the Nyquist criterion is satisfied. In the fifth-order experiment the spacing along both axes was generally 12 fs. This corresponds to a Nyquist critical frequency of $\sim$1400 cm^{-1}, and the Nyquist frequency criterion is still satisfied. We choose not to spline these data because it may introduce bias and because it makes the fifth-order deconvolution relatively costly in time. In general, oscillations around the Nyquist critical frequencies have not been problematic until the division steps present in all of the deconvolutions are performed. In the heterodyne deconvolution the FT signal is divided once by the FT autocorrelation profile, in the homodyne third-order deconvolution FT data is divided twice by the FT assumed pulse intensity profile, and in the homodyne fifth-order deconvolution FT data is divided three times by the FT pulse intensity profile. The problem of high frequency divergences after division is not explicitly addressed in the papers introducing and discussing the third-order heterodyne deconvolution procedure [25,29–33]. We found two sources of high frequency divergences. The first is the different Nyquist oscillations in the FT data and FT autocorrelation (or pulse intensity) functions, so that when dividing the former by the latter, high frequency divergences result. The second is related to use of an assumed pulse function (so this need not apply to the heterodyne deconvolution, but does apply to the homodyne deconvolutions): because noise is only present in the dividend of the division, the pulse profile approaches zero faster than the data, and high frequency divergences are artificially introduced. We have removed those specious contributions by cutting off the frequency domain data at the point where the divergences begin and extending the data in a straight line (for positive and negative frequencies greater than the absolute value of the cut-off frequency) beyond that point. This results in some loss of information at early times, but we have attempted to leave the frequency cut-offs high enough so that there is limited effect on the separation of the electronic and nuclear portions of the response.

Of course, this same problem appears three times in the fifth-order deconvolution. The problem is compounded by the nature of the collected fifth-order signal. Here a signal behind $\tau_2 = 0$ fs that is not related to the response function ($R(s_1, s_2)$ as presented in Section 2 of this paper) governing the signal in the front quadrant ($\tau_2 > 0$ fs) appears [21,24]. The signal in the back quadrant ($\tau_2 < 0$ fs) is the fifth-order signal describing when pulses three and four impinge upon the sample before pulses one and two impinge upon the sample a time τ_2 later. If the polarizations of beams three and four differ from those of beams one and two, clearly the tensor element measured in the back quadrant is different from that in the front quadrant. Further, the signal in the back quadrant has more contributions from cascades than does that in the front quadrant. The phase-matching geometry used to collect direct fifth-order signal was designed to discriminate against cascades for the geometry giving rise to signal in the front quadrant. Because the geometry is asymmetric the phase-matching numbers governing signal in the front quadrant need not govern that in the back quadrant. The phase-matching numbers for the back quadrant show greater contributions from symmetric cascades and less from direct fifth-order signal than do those governing the front quadrant [43]. While Ref. [21] showed that all presented tensor elements in the front quadrant were dominated by direct fifth-order signal, that can not be assumed for signal in the back quadrant. However, we can not simply artificially cut the data off at $\tau_2 = 0$ fs because the discrete Fourier transform of such signals artificially introduces false amplitude offsets in the frequency domain. Instead, the signal measured in the front quadrant was extrapolated behind $\tau_2 = 0$ fs to follow the pulse profile, and this signal was used as the signal to Fourier transform. However, when deconvoluting this signal we found oscillations were introduced by the abrupt fall off of the signal behind time zero. As a result, instead of extrapolating the front quadrant data as described, we flipped the data set in the front quadrant, placed it in the back quadrant, and allowed it to

remain there during the deconvolution procedure. This resulted in reconvolutions that fit the measured signal as well as did those performed in the manner described above. Moreover, it led to fewer oscillations in the deconvoluted $R(t)$ since the signal in the back quadrant acted as an effective filter for data along the τ_2 dimension. Thus, all fifth-order deconvolutions were performed in this way.

Even using this procedure we can not avoid introducing several small inaccuracies in the fifth-order deconvolution procedure. First, we are not accounting for the small amount of back quadrant signal that leaks into the front quadrant. Second, the signal in the back quadrant will carry a different phase than that in the front quadrant, and some interference around $\tau_2 = 0$ fs may be present in the measured surfaces and this can not currently be accounted for. A more sophisticated theory, which accounts for the presence of a second response function that occupies the $\tau_2 < 0$ fs, $\tau_4 > 0$ fs portion of the measured response, could be developed, but this has not been attempted yet. Behind the $\tau_4 = 0$ fs axis there is no signal due to another response function, and therefore these approximations do not enter in that dimension. However, because behind $\tau_4 = 0$ fs the measured signal falls off with the pulse profile, we have no effective filter in this dimension, and that leads to oscillations in the deconvoluted signal along the τ_4 dimension.

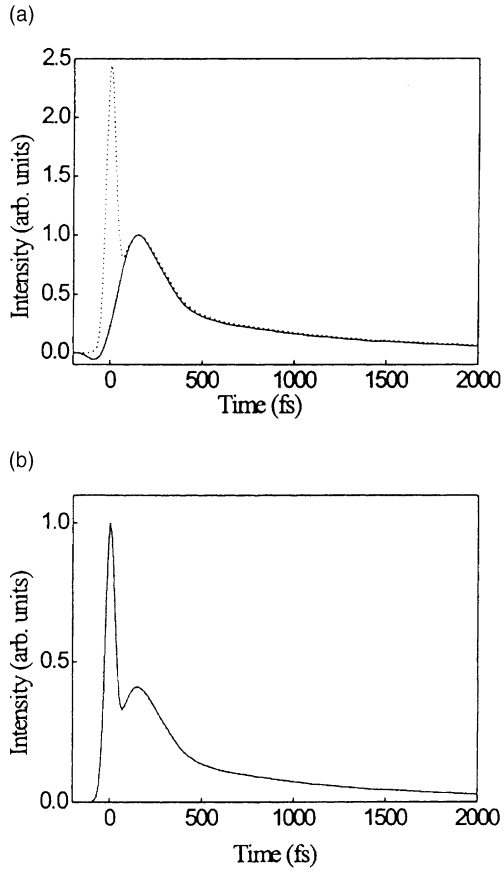

Fig. 2. (a) Heterodyne detected R_{zzzz} measurement (···) and deconvoluted R_{zzzz} (—). (b) Heterodyne detected R_{zzzz} measurement (···) and reconvoluted R_{zzzz} (—).

4.2. Examples

4.2.1. Third-order signals

As discussed above, we first perform the deconvolution on third-order heterodyne detected (non-phase selected) R_{zzzz} data. The procedure was performed according to the procedure of McMorrow et al. The deconvoluted signal was then reconvoluted with the autocorrelation function to ensure that the collected signal could be reproduced. Fig. 2 shows the results of the deconvolution, $R(t)$, as well as the collected signal, $S(t)$, and the reconvoluted signal. In this deconvolution, $R^{(3)}(\omega)$, the Fourier transform of the data divided by the Fourier transform of the autocorrelation function was truncated at 252 cm^{-1} to prevent high frequency divergences from falsely influencing the inverse transform that gives $R^{(3)}(t)$. The choice of frequency at which to truncate the data was made keeping various factors in mind. Ref. [34] states that the real part of $R(\omega)$ should be flat and that the imaginary part of $R(\omega)$ should be flat and zero at high frequencies if the deconvolution procedure is proceeding properly. The cut-off frequency was chosen such that these conditions are satisfied after $R(\omega)$ is truncated at the selected point and then extended from that point in a straight line. Further, because there is some uncertainty in the relative time zeros of the measured signal and autocorrelation, the time zero of the autocorrelation function was held constant while the zero of the measured signal was treated

as a variable parameter. The choice of time zero was made so as to make the baseline of the imaginary part of $R(\omega)$ as close to zero as possible. The DC offset in Re $R(\omega)$ was also removed. This offset has been shown to be related to the electronic response in third-order [25,29], thus removing this offset effects the removal of the hyperpolarizability (γ_{lkji}) spike at time zero in the inverse transform of $R(\omega)$. While the frequency cut-off appears rather low considering that our pulse excites a bandwidth of $\sim$600 cm^{-1}, the reconvolution, which does reproduce the measured signal, shows that crucial information is retained.

The heterodyne deconvolution according to the procedure of McMorrow et al. has also been performed using an assumed autocorrelation shape instead of the measured autocorrelation function. Fig. 1 shows the measured autocorrelation along with its fits to the autocorrelation functions corresponding to Gaussian and sech^2 intensity pulse profiles. Deconvolutions were performed with both assumed pulse shapes and no significant differences were seen. Fig. 3 shows the $R(t)$ obtained from the deconvolution using the measured autocorrelation and the assumed Gaussian. This result bodes well for the homodyne deconvolution where intensity pulse shapes are assumed.

Next, we deconvoluted the R_{zzzz} homodyne detected third-order data. This is the first time to our knowledge that such a procedure has been performed on third-order non-resonant homodyne

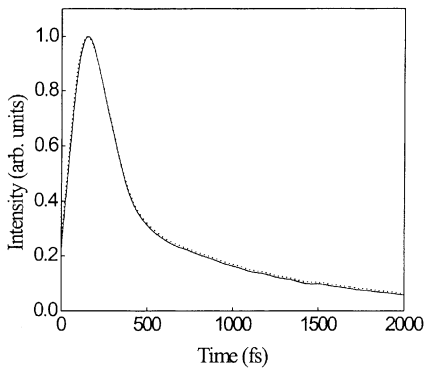

Fig. 3. Deconvoluted heterodyne detected R_{zzzz} data (···) using a Gaussian with intensity FWHM of 43 fs and deconvoluted heterodyne detected R_{zzzz} data (—) with the measured autocorrelation function.

detected data. This convolution necessitates two divisions by FT pulse profiles, and therefore the problems with high frequency divergences appear twice. The assumed pulse intensity profile used was a Gaussian with FWHM of 60 fs. This was deduced from the measured autocorrelation function that, like the one shown in Fig. 1, was fairly well fit by a Gaussian. (The heterodyne and homodyne detected third-order experiments were performed with significantly different laser conditions.) After the first division the frequency was cut-off and extrapolated after 519 cm^{-1}. After the second division the frequency was cut-off and extrapolated after 196 cm^{-1}. As in the heterodyne deconvolution the zero of the signal was varied to get the offset of Im $R(\omega)$ as close to zero as possible. Again, a reconvolution was satisfactorily performed. The measured and reconvoluted signal, along with the deconvoluted $R(t)^2$ (the square of the response is shown for comparison with the measured signal) are shown in Fig. 4.

While the $R(t)$'s obtained from the heterodyne and homodyne deconvolutions (Fig. 5) and reconvolutions do reproduce the measured signals almost exactly in both cases, when we compare the $R(t)$'s obtained from the heterodyne and homodyne deconvolutions we find a slight difference in behavior. Because of the two frequency cut-offs in the homodyne deconvolution procedure, the homodyne deconvolution is less likely to be exact since we are losing more information in the short time region. Indeed, while the deconvoluted response functions are expected to be zero at time zero, neither the heterodyne nor homodyne results are exactly zero, most likely due to the frequency cut-offs. Another explanation is the presence of (different amounts of) imaginary components in both the heterodyne detected and homodyne detected signals and deconvoluted $R(t)$'s.

Despite the small difference between the $R(t)$'s obtained with the heterodyne and homodyne deconvolutions, the homodyne deconvolution procedure does appear satisfactory, if imperfect, in recovering $R(t)$, though further study would be necessary to determine whether this is the case in liquids where the dichroic response is greater than in CS_2. Further, because the formalism presented in Section 2 of this paper does appear to give

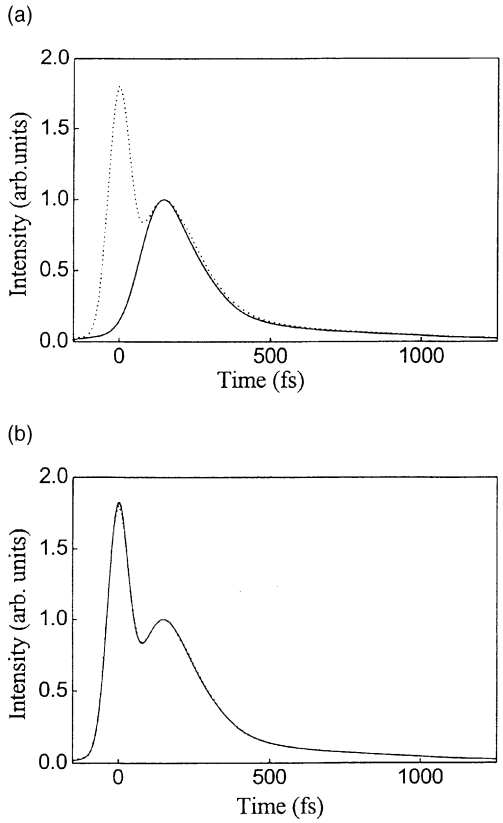

Fig. 4. (a) Homodyne R_{zzzz} measurement (···) and deconvoluted R^2_{zzzz} (—). The square of $R(t)$ is plotted to compare to the measured homodyne detected signal. (b) Homodyne R_{zzzz} measurement (···) and reconvoluted R^2_{zzzz} (—).

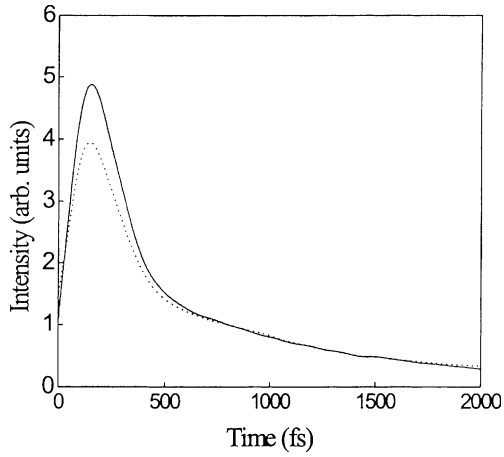

Fig. 5. R_{zzzz} from the heterodyne deconvolution (—) (also seen in Fig. 3a) and from the homodyne deconvolution (···) (seen as R^2_{zzzz} in Fig. 4a). The discrepancy in these response functions is discussed in the text.

satisfactory results in third-order, the procedure can be used with some level of confidence for the fifth-order signal.

As we move to fifth-order deconvolutions, we have shown that the assumption of a pulse shape based on a measured autocorrelation function is likely unimportant, though we have not shown that the presence of imaginary components in the measured signal negligibly affects the bare $R(t)$. We must also bear in mind that the fifth-order deconvolution has other complexities as discussed in Section 4.1.

4.2.2. Fifth-order signals

The fifth-order homodyne deconvolution was performed in accordance with Section 2 of this paper. There are three points (two in the frequency corresponding to τ_4 and one in the frequency corresponding to τ_2) at which FT data is divided by a FT pulse profile, and we find that we must employ frequency cut-offs at each of these points. Unlike in the third-order data, in the fifth-order experiment there are many slices of frequency domain data, and each behaves differently. Instead of using a variable cut-off, in which each slice is cut at a different frequency according to the criteria set out in the third-order deconvolutions, we have chosen to use one cut-off that is acceptable for all slices, generally resulting in flat real and imaginary portions of the frequency domain result after division. This is an imperfect procedure, but varying the frequency cut-off for each slice makes the fifth-order deconvolution excessively time consuming. In the case of the polarized signal, R_{zzzzzz}, the same frequency cut-off, 320 cm^{-1}, was used each time a cut-off was applied. These frequency cut-offs do not unduly affect the deconvolution, as we can perform a reconvolution with a satisfactory result. The reconvoluted signal reproduces the measured signal qualitatively as is seen in Fig. 6a and c. On a more quantitative level, we see that slices taken along the reconvoluted signal at $\tau_2 = 120$ fs and $\tau_4 = 60$ fs (near the peak of the measured signals along each dimension) match up quite well with

those of the measured signal. Small differences do exist however, mainly in the short time response along τ_2, and this is possibly due to the employment of the frequency cut-offs. The slice along τ_2 of the deconvoluted signal presented in Fig. 7a (the square of the response function $R(t)$ is shown for comparison with the measured signal: this will be the case for every fifth-order deconvoluted surface and slice shown in this paper) also appears to overestimate the contribution at time zero. This, however, is not the most obvious problem with the deconvoluted signal. Fig. 6b displays the deconvoluted R_{zzzzzz} signal. The deconvoluted signal is obviously of much lower quality (lower signal to noise and evident oscillations) compared to the third-order deconvoluted signals. The noise in the deconvoluted signal is related to the fact that the direct fifth-order signal is exceedingly small. In addition, because data collection times are quite lengthy, the signals are not measured in both dimensions to times long enough for all signal to decay to zero. The abrupt drop in signal in certain slices of the measured signals may introduce offsets and oscillations in the FT data, which contribute

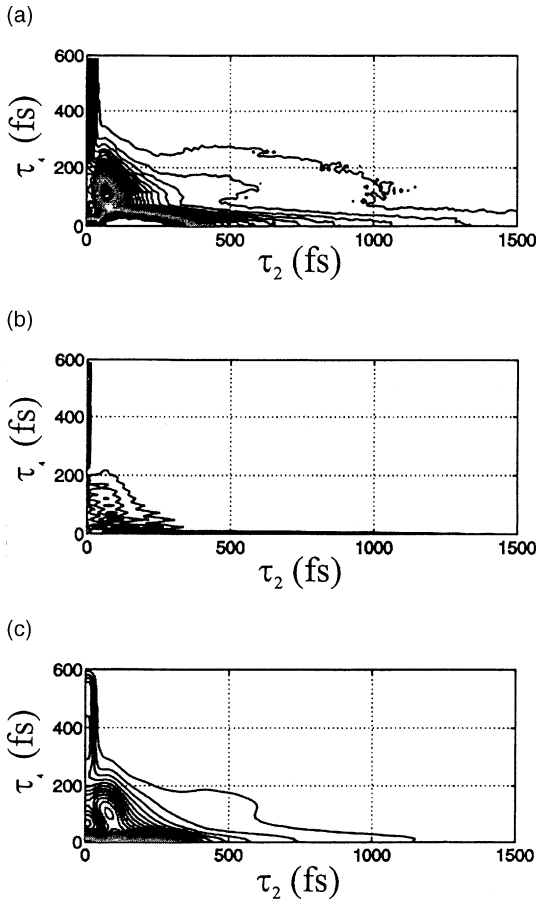

Fig. 6. (a) Measured, (b) deconvoluted (R^2), and (c) reconvoluted R_{zzzzzz} signals.

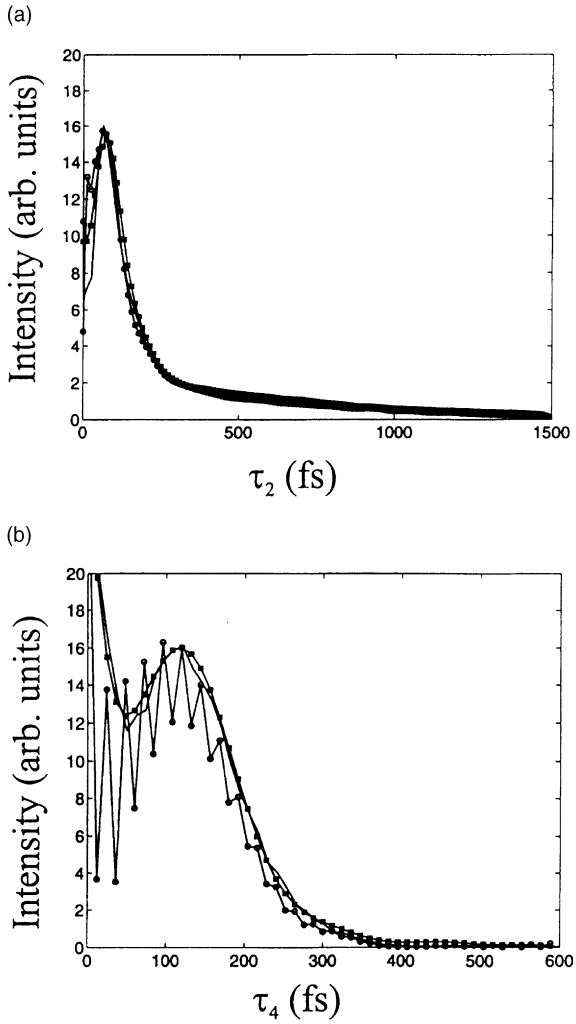

Fig. 7. (a) Measured (—), deconvoluted (–●–) (R^2), and reconvoluted (–■–) R_{zzzzzz} signals at $\tau_4 = 120$ fs. They have been scaled to be of equal amplitude at $\tau_2 = 80$ fs. (b) Measured (—), deconvoluted (–●–) (R^2), and reconvoluted (–■–) R_{zzzzzz} signals at $\tau_2 = 60$ fs. They have been scaled to be of equal amplitude at $\tau_4 = 120$ fs.

to the noisiness of the deconvoluted data. Oscillations are evident in the slice taken along τ_4 and presented in Fig. 7b. This slice suffers significantly more from oscillations than does the slice along τ_2 for two reasons. First, while neither the collected signal near the τ_2 nor τ_4 axes decay to zero at long τ_2 or τ_4, this is especially true of the slice along τ_4, and this may lead to Gibbs oscillations [44]. Second, the slice along τ_4 drops off quickly behind time zero while along τ_2 the signal in the back quadrant acts as an effective filter for the Fourier transforming of the measured signal. Note that unlike in the third-order signal, we have chosen not to remove the DC components of the slices of Re $R(\omega)$.

As in the third-order signal, comparing slices from the measured and deconvoluted fifth-order signals reveals that in the case of CS_2 even for the fifth-order signal, where five pulses potentially overlap, the deconvoluted signal does not have significantly different features than the measured signal. The slice at $\tau_4 = 120$ fs peaks slightly earlier than does that of the measured signal (70 vs. 80 fs). The effect is greater in the slice at $\tau_2 = 60$ fs (peak at ~95 vs. 120 fs). While these movements are likely real, because the reconvolution is not exact and the oscillations in the deconvoluted signal along τ_4 make it difficult to ascertain the location of the peak, the magnitude of these shifts is difficult to quantify.

Similar results were found for the other deconvolutions performed. These were performed on the fifth-order tensor elements R_{zzmmzz} and R_{yzzzzy} as well as on a measured parallel cascade signal. The two direct fifth-order tensor elements were chosen because these show some of the most interesting behaviors among the tensor elements that have been measured [21]. It was suggested that the R_{zzmmzz} tensor element would select for echo-like pathways [10,11]. It was shown that indeed this tensor element does extend further along the diagonal ($\tau_2 = \tau_4$ fs) than any other tensor element of the direct fifth-order signal. The extension along the diagonal is indicative of an echo, and the R_{zzmmzz} signal (Fig. 8a) has allowed us to put a lower limit of ~400 fs on the timescale of "inhomogeneity" of room temperature CS_2 [24]. The presence of the signal along the diagonal indicates

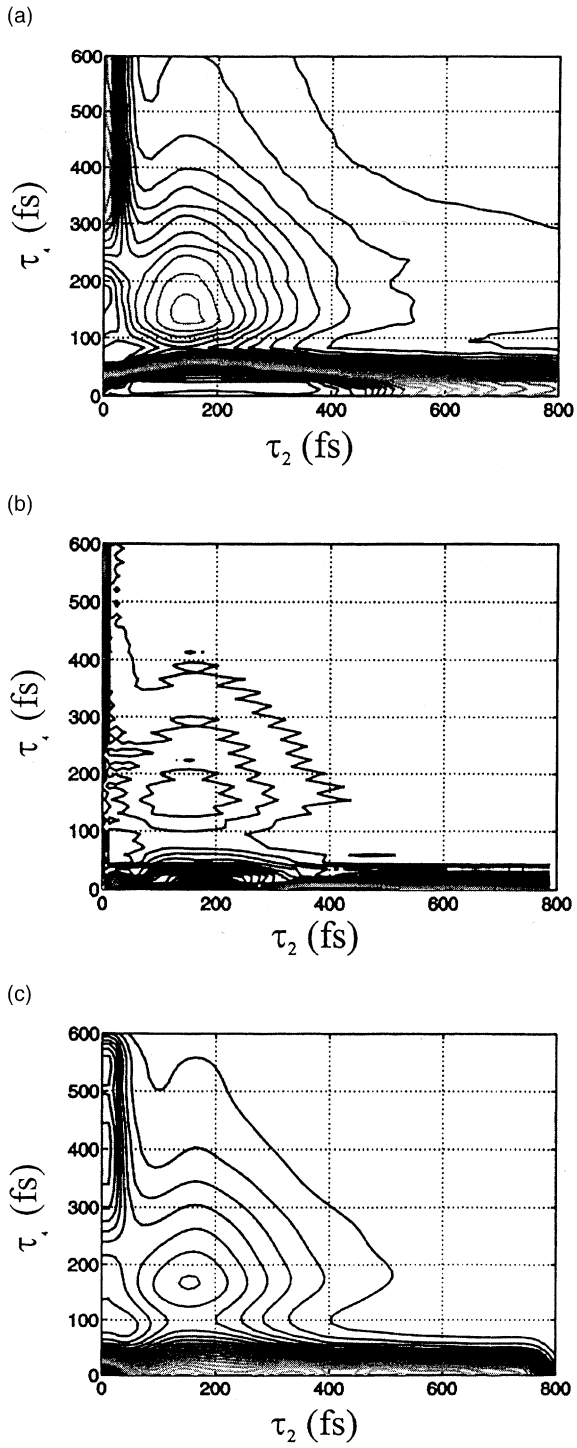

Fig. 8. (a) Measured, (b) deconvoluted (R^2), and (c) reconvoluted R_{zzmmzz} signals.

that there is meaning in using the language of modes to discuss intermolecular motions, for there are motions that retain memory of their original frequency for several hundred femtoseconds. However, these timescales are on the order of the inverse frequencies of these modes, so it may be inappropriate to use the term inhomogeneity to describe this behavior. The R_{yzzzzy} signal (Fig. 11a) has been shown to extend along the τ_4 dimension in a way none of the other tensor elements do. The behavior of this tensor element is unique and potentially relates to the presence of population dynamics information in the fifth-order signal. The presence of the extended feature along both $\tau_2 = 0$ fs and $\tau_2 \sim 150$ fs, together with the decay along τ_2, show the potential of the direct fifth-order signal to reveal population and dephasing timescales in one measurement.

The measured, deconvoluted, and reconvoluted R_{zzmmzz} signals are shown in Fig. 8a–c, respectively. The frequency cut-offs employed in this deconvolution were 360, 330, and 300 cm^{-1}. The reconvoluted signal matches up to the measured signal at least as well as that shown for the R_{zzzzzz} signal. The ($\tau_4 = 150$ fs, $\tau_2 = 180$ fs) slices shown in Fig. 9a and b both show that the deconvoluted signal peaks slightly later than the measured signal. This peak movement is small and difficult to quantify for the same reasons discussed for the R_{zzzzzz} slices, though it is opposite in direction from that seen in the R_{zzzzzz} slices, and thus is unexpected.

Fig. 10 shows the diagonal slices from the measured and deconvoluted R_{zzzzzz} and R_{zzmmzz} tensor elements. As is true of the slices of these respective tensor elements, the deconvoluted R_{zzzzzz} diagonal peaks earlier than does the measured signal. The opposite effect is seen in the R_{zzmmzz} tensor element. Despite the later peak in the R_{zzmmzz} signal, the two diagonals (R_{zzmmzz} and deconvoluted R_{zzmmzz}) decay on the same timescale, and therefore our conclusions placing a lower bound on the "inhomogeneity" of room temperature CS_2 do not change with the examination of the bare nuclear response function.

Fig. 11a and b show the measured and deconvoluted R_{yzzzzy} signals. The frequency cut-offs employed here were 267, 267, and 320 cm^{-1}. Though these cut-offs are somewhat lower than that for

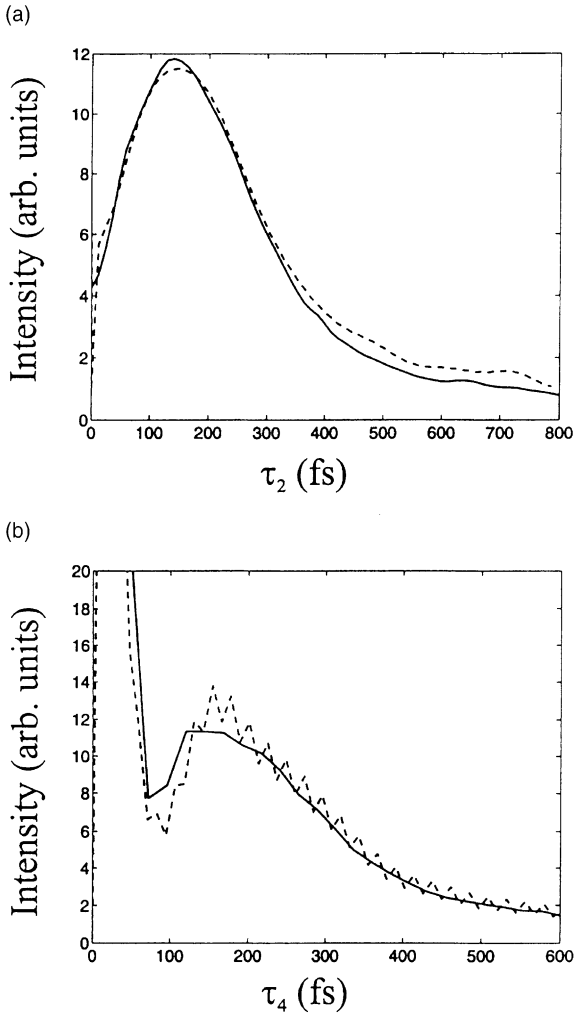

Fig. 9. (a) Measured (—) and deconvoluted (- - -) (R^2) R_{zzmmzz} signals at $\tau_4 = 150$ fs scaled at $\tau_2 = 180$ fs. (b) Measured (—) and deconvoluted (- - -) (R^2) R_{zzmmzz} signals at $\tau_2 = 180$ fs scaled at $\tau_4 = 140$ fs.

other fifth-order deconvolutions, the reconvoluted signal matches up very well with the measured signal. Though the deconvoluted signal looks to have lost the interesting feature extending along τ_4, this is not the case as can be seen in Fig. 11d, which depicts a slice along that dimension. Instead, it is the relative height of the peak at time zero to the rest of the response that makes the contour plot of the deconvoluted signal appear to lose the extension along τ_4. The difference in intensities is to be expected as the deconvolution

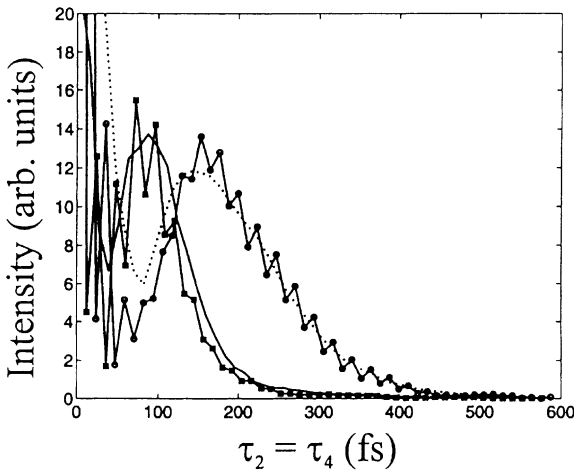

Fig. 10. Diagonal slices from measured (—) and deconvoluted (R^2) (–■–) R_{zzzzzz} signals as well as from measured (···) and deconvoluted (R^2) (–●–) R_{zzmmzz} signals.

compresses the area under the broadened electronic portion of the measured response into a much smaller area at or around time zero. Interestingly, the lean towards the $\tau_2 = 0$ fs axis with increasing τ_4 persists after deconvolution, showing that this aspect of the measured signal (implying that as τ_4 increases higher frequency motions are weighted more heavily) is likely not an artifact of the convolution with the electronic response along the $\tau_2 = 0$ fs axis, though again, inaccuracies at short times could contribute to the persistence of this feature.

While in third-order the main value of the deconvolution procedure is in revealing the bare nuclear response function, in fifth-order there is the further result of revealing the hyperpolarizability responses that should be compressed to the axes after deconvolution. While the frequency cut-offs prevent complete compression of the hyperpolarizability responses onto the axes, we believe that what results on the axes are good approximations of the true hyperpolarizability response looks like. Fig. 12a shows the $\tau_4 = 0$ fs hyperpolarizability response ($\langle[\gamma_{zzzz}(\tau_2), \alpha_{zz}(0)]\rho\rangle$) from the deconvoluted R_{zzzzzz} direct fifth-order measurement as well as the $\tau_4 = 0$ fs response from a deconvoluted R_{zzzzzz} measured parallel cascade signal. The deconvoluted cascade signal was not shown, but the deconvolution has been performed using frequency cut-offs of 360, 240, and 167 cm^{-1}. The reconvoluted signal matches almost quantitatively with the measured signal, though at the earliest times there are small discrepancies. As shown in Eq. (18), the deconvoluted parallel R_{zzzzzz} signal should reveal $R_{zzzz}(\tau_2 + \tau_4) \times R_{zzzz}(\tau_2)$. So, taking a slice along $\tau_4 = 0$ fs of the deconvoluted cascade signal should reveal a deconvoluted third-order $R_{zzzz}(t)^2$ measurement, and indeed the slice taken along the $\tau_4 = 0$ fs axis has all the features of the third-order deconvoluted signals. There are discrepancies in peak position, peak width, and decay times, but these are small and can be explained by any of the number of implementation difficulties affecting the two-dimensional deconvolutions. On the other hand, the slice along $\tau_4 = 0$ fs taken from the measured R_{zzzzzz} direct fifth-order signal reveals not a slice of third-order data, but instead a hyperpolarizability. This hyperpolarizability signal can not be measured with a lower-order technique, and without deconvolution it extends into the true two-dimensional area of the measured signal, potentially contaminating and being contaminated by the direct fifth-order nuclear response. The hyperpolarizability response probes similar dynamics to third-order non-resonant experiments, and therefore it was believed that the hyperpolarizability responses might resemble third-order measurements. We can clearly see that the measured hyperpolarizability response does not mirror the third-order response (or the slice along $\tau_4 = 0$ fs from the cascade measurement). Even with errors that may occur from our implementation of the fifth-order deconvolution procedure, we can say with confidence that the hyperpolarizability function decays on a slower time scale than does the third-order signal and that it peaks later than the third-order signal.

While in the measured response any signal present at time $\tau_4 = 0$ fs must be due to hyperpolarizability signal, this is not the case for signal present along the $\tau_2 = 0$ fs axis. Instead, it has been shown that both a hyperpolarizability signal, described by a $\langle[\alpha_{nm}(\tau_4), \gamma_{lkji}(0)]\rho\rangle$ interaction, as well as a fifth-order signal governed by a three-point polarizability correlation function can populate this axis. The fifth-order signal governed by

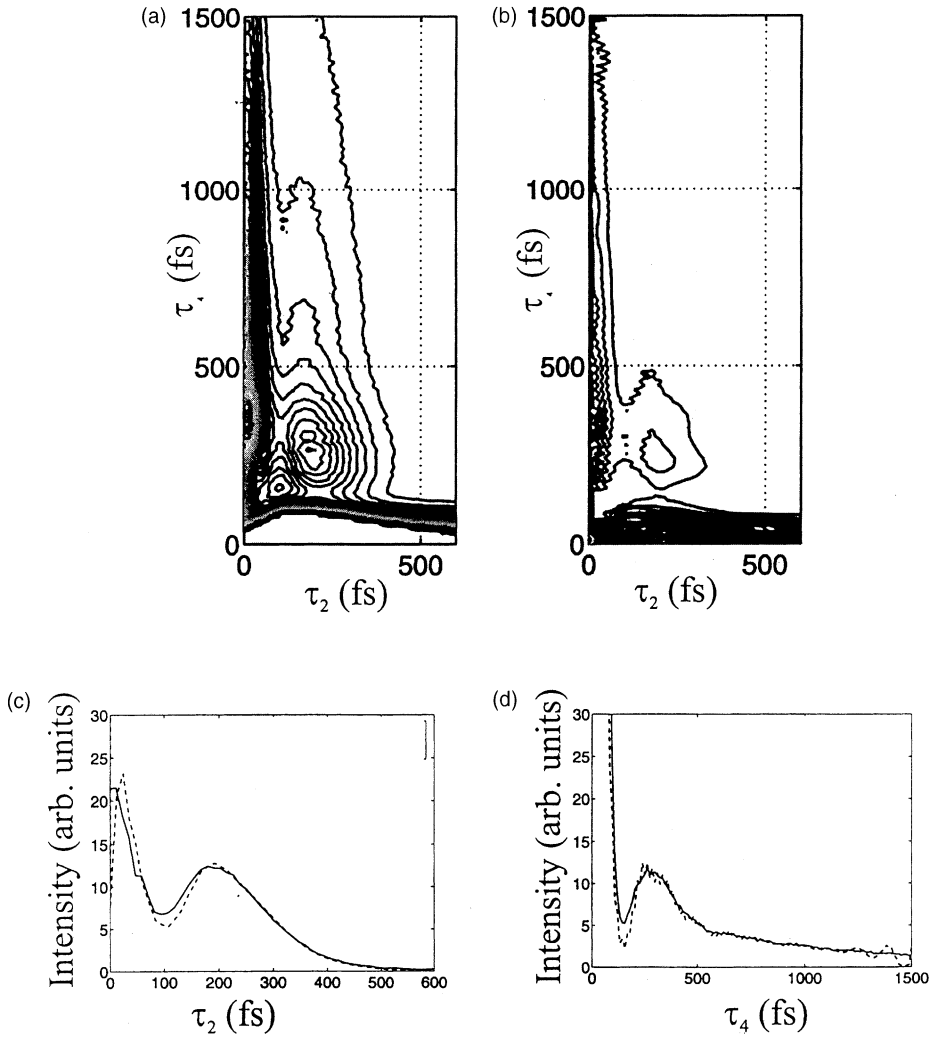

Fig. 11. (a) Measured and (b) deconvoluted (R^2) R_{yzzzzy} signals. (c) Slices from the measured (—) and deconvoluted (- - -) (R^2) R_{yzzzzy} signals at $\tau_4 = 250$ fs scaled at $\tau_2 = 180$ fs. (d) Slices from the measured (—) and deconvoluted (- - -) (R^2) R_{yzzzzy} signals at $\tau_2 = 160$ fs scaled at $\tau_4 = 250$ fs.

$\langle[[\alpha_{nm}(\tau_4), \alpha_{kl}(\tau_2)], \alpha_{ji}(0)]\rho\rangle$ that can exist on this axis is only fifth-order signal that describes population dynamics [15,21]. While most direct fifth-order tensor elements measured have shown significant long-lived signal along and around this axis, this long-lived feature is most obvious in the R_{yzzzzy} signal, where there is both significant signal along that axis as well as signal off the axis but also extending along τ_4. It has been suggested that this feature of the R_{yzzzzy} signal describes population dynamics and that this tensor element of the direct fifth-order signal appears to weight for population-type pathways in much the same way that R_{zzmmzz} appears to weight for echo-like pathways [21]. So, after deconvolution, the remaining signal on the $\tau_2 = 0$ fs axis of any of the fifth-order measurements should include both a hyperpolarizability and fifth-order three-point polarizability signal, though we might expect the hyperpolarizability to dominate, since the deconvolution ideally compresses all of the hyperpolarizability's area onto the axis. Fig. 12b displays slices along

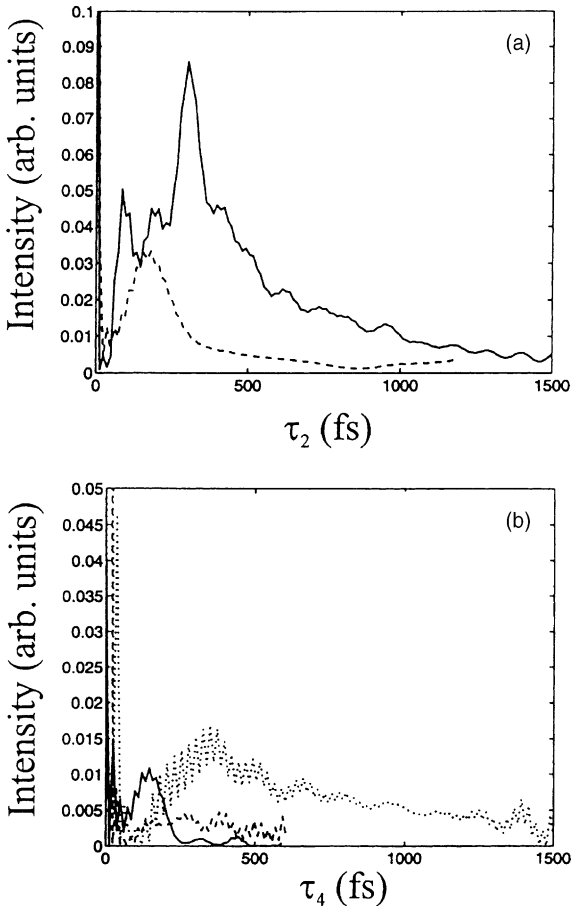

Fig. 12. (a) Hyperpolarizabilities at $\tau_2 = 0$ fs from the R_{zzzzzz} deconvoluted (R^2) direct fifth-order (—) and R_{zzzzzz} cascade (- - -) signals. (b) Hyperpolarizabilities at $\tau_4 = 0$ fs from the deconvoluted (R^2) R_{zzzzzz} (—), R_{zzmmzz} (- - -), and R_{yzzzzy} ($\cdots$) signals.

$\tau_2 = 0$ fs taken from the deconvoluted R_{zzzzzz}, R_{zzmmzz}, and R_{yzzzzy} direct fifth-order signals. Interestingly the slice along that dimension from the R_{zzzzzz} signal resembles a third-order signal more than it does the hyperpolarizability along the $\tau_4 = 0$ fs axis shown in Fig. 12a, though the two hyperpolarizabilities are governed by the similar correlation functions, $\langle[\alpha_{zz}(\tau_4), \gamma_{zzzz}(0)]\rho\rangle$ and $\langle[\gamma_{zzzz}(\tau_2), \alpha_{zz}(0)]\rho\rangle$. Contamination of the measured fifth-order signal by cascades may play a larger role along the axes than elsewhere, and that contamination may be evident in this slice of the R_{zzzzzz} tensor element. Unlike the R_{zzzzzz} slice along $\tau_2 = 0$ fs, the R_{zzmmzz} deconvoluted slice at $\tau_2 = 0$ fs appears to have significant signal out until 600 fs and appears to decay quite slowly. This may be an indication of the presence of population dynamics information in this slice. The slice taken on the $\tau_2 = 0$ fs axis from the R_{yzzzzy} signal, governed by $\langle[\alpha_{yz}(\tau_4), \gamma_{zzzy}(0)]\rho\rangle$ and $\langle[[\alpha_{yz}(\tau_4), \alpha_{zz}(\tau_2)], \alpha_{zy}(0)]\rho\rangle$ (note that third-order $\langle[\alpha_{zz}(t), \alpha_{zy}(0)]\rho\rangle$ response similar to γ_{zzzzy} would be zero) appears to be quite long-lived. Interestingly, it resembles the $\langle[\gamma_{zzzz}(\tau_2), \alpha_{zz}(0)]\rho\rangle$ signal in Fig. 12a, though along this axis it is unclear whether this signal is due to the hyperpolarizability response, population dynamics, or a combination of the two. While this is true of the signal on the $\tau_2 = 0$ fs axis, the extended deconvoluted R_{yzzzzy} response near the $\tau_2 = 0$ fs axis is suspected to arise from population dynamics alone.

4.3. Future use

While the results presented for the direct fifth-order signal are not as satisfactory as those for the third-order signal, the deconvolution procedure shows promise for examining the fifth-order response function directly in future homodyne detected fifth-order experiments. Several improvements that can be made both to the technique and the data collection procedure should improve the outcome of the deconvolution procedure. In terms of technique, there are more sophisticated ways of frequency filtering than employing one frequency cut-off for all slices: however, until this is combined with higher quality data and data taken at shorter time intervals and to longer times along both dimensions, it will be difficult to obtain clean bare nuclear response functions from the data. Of course, at present, collecting direct fifth-order data is difficult experimentally, and taking smaller time steps over the course of a whole surface as well as taking such steps in each dimension to long times may lead to data collection times that are prohibitively long. Another issue that could affect the results presented here and could be remedied with changes to the experimental setup is the presence of residual cascade signals in the measured data. While our phase-matching geometry discriminates quite effectively against cascade signals in the front

quadrant, a better one could potentially be found. Further, finding a geometry that both discriminates effectively vs. the cascades and is symmetric would be helpful because it would assure us that no cascade signals from the back quadrant would leak into the front quadrant and that no interferences around time zero from the phase differences between potential cascades and direct fifth-order signal would contribute to the measured signal.

Further, in the near future attempts will be made to collect direct fifth-order data with shorter pulses so that high-frequency vibrations are excited and the couplings between intramolecular modes as well as between intramolecular and intermolecular modes can be studied. Because of the spectral filtering that occurs when using finite duration pulses, the high frequency modes will be weighted less heavily than they would otherwise be. This will clearly become an important issue when choosing to look at the frequency domain Fourier transformed direct fifth-order signal to determine information regarding the couplings between different high frequency vibrations. In this case spectral filtering could potentially lead to incorrect interpretations of the nature and magnitude of these interesting couplings, and here the homodyne deconvolution technique may prove useful.

Of course, the problems implementing the deconvolution procedure for homodyne detected fifth-order measurements is yet another reason to attempt to collect phase-selected heterodyne detected fifth-order data. Several groups are already pursuing this goal in an attempt to increase the level of fifth-order signal as well as to completely remove cascade contributions [22,23]. To remove cascade contributions in this way requires the use of active or passive phase-locking and the ability to collect the real and imaginary portions of the signal separately. With a new phase-sensitive technique and the accompanying cascade-free fifth-order signal collected, the deconvolution procedure will likely prove more effective. Of course, the phase sensitive detection will be a heterodyne detection so that the deconvolution procedure will necessarily be modified from that presented here and would be capable of retrieving both the absolute sign and phase of the nuclear response function.

5. Conclusion

We have presented a deconvolution procedure for use on fifth-order homodyne detected signals that ideally confines the electronic response of the system to the two time axes. In doing so, an analogous procedure was first developed for non-resonant third-order homodyne detected data (which ideally confines the electronic response of the system to time zero). The third-order homodyne deconvolution was compared to the well-known third-order heterodyne deconvolution, and the results were shown to be very similar. The discrepancies between the two deconvolutions are likely due to the need for two frequency cut-offs in the homodyne deconvolution as well as to the presence of small (and perhaps different) amounts of imaginary signals in the third-order heterodyne and homodyne detected data. These results suggest that one must be careful not to use the homodyne deconvolution procedure on a system in which the dichroic response is large. The deconvolution developed for the fifth-order homodyne detected signal was employed on three measured tensor elements of the direct fifth-order signal as well as on one tensor element of a measured parallel cascade signal. The fifth-order deconvolution employs three frequency cut-offs, and these cut-offs along with experimental limitations lead to slight discrepancies between the measured and reconvoluted fifth-order signals. Even if we had reconvoluted the deconvoluted signals perfectly, we would still be unsure that the resulting signal was the bare nuclear response function describing birefringence, since dichroic parts of the response may also appear in the deconvoluted signal as they did in third-order. As in third-order, the fifth-order deconvolutions did not result in the peak of the responses moving significantly from where they appeared in the measured signal: thus, for the case of CS_2 the nuclear response appears sufficiently slow in both third- and fifth-order data so that using 40–60 fs pulses does not unduly affect the nuclear portion of the response. However, even for

CS_2 the fifth-order homodyne deconvolution is useful for helping to reveal features of the hyperpolarizability responses that ideally become confined to the τ_2 and $\tau_4 = 0$ fs axes after deconvolution.

Acknowledgements

This work was supported by the NSF (USA) and the CRI program of KISTEP (MOST, Korea). J. Sung is supported by a postdoctoral fellowship from the Korea Science and Engineering Foundation (KOSEF). The authors gratefully acknowledge Dr. Mino Yang for helpful suggestions and insightful comments.

References

[1] Y. Tanimura, S. Mukamel, J. Chem. Phys. 99 (1993) 9496.
[2] V. Chernyak, S. Mukamel, J. Chem. Phys. 108 (1998) 5812.
[3] V. Chernyak, A. Piryatinski, S. Mukamel, Laser Chem. 19 (1999) 109.
[4] T. Steffen, J.T. Fourkas, K. Duppen, J. Chem. Phys. 105 (1996) 7364.
[5] K. Okumura, Y. Tanimura, J. Chem. Phys. 107 (1997) 2267.
[6] K. Okumura, Y. Tanimura, J. Chem. Phys. 106 (1997) 1687.
[7] S. Mukamel, A. Piryatinski, V. Chernyak, J. Chem. Phys. 110 (1999) 1711.
[8] S. Mukamel, A. Piryatinski, V. Chernyak, Acc. Chem. Res. 32 (1999) 145.
[9] M. Cho, in: S.H. Lin, A.A. Villaeys, Y. Fujimura (Eds.), Advances in Multi-Photon Processes, Spectroscopy, vol. 12, first ed., World Scientific, Singapore, 1999, p. 229.
[10] R.L. Murry, J.T. Fourkas, J. Chem. Phys. 107 (1997) 9726.
[11] R.L. Murry, J.T. Fourkas, T. Keyes, J. Chem. Phys. 109 (1998) 7913.
[12] T. Steffen, K. Duppen, Chem. Phys. Lett. 273 (1997) 47.
[13] T. Steffen, K. Duppen, Phys. Rev. Lett. 76 (1996) 1224.
[14] T. Steffen, K. Duppen, Chem. Phys. Lett. 290 (1998) 229.
[15] T. Steffen, K. Duppen, Chem. Phys. 233 (1998) 267.
[16] A. Ma, R. Stratt, Phys. Rev. Lett. 85 (2000) 1004.
[17] S. Saito, I. Ohmine, J. Chem. Phys. 108 (1998) 240.
[18] D. Blank, L. Kaufman, G.R. Fleming, J. Chem. Phys. 111 (1999) 3105.
[19] J.C. Wright, J.E. Ivanecky, Chem. Phys. Lett. 206 (1993) 437.
[20] D.J. Ulness, J.C. Kirkwood, A.C. Albrecht, J. Chem. Phys. 108 (1998) 3897.
[21] L. Kaufman, D.A. Blank, G.R. Fleming, J. Chem. Phys. 114 (2001) 2312.
[22] V. Astinov, K.J. Kubarych, C.J. Milne, R.J.D. Miller, Chem. Phys. Lett. 327 (2000) 334.
[23] O. Golonzka, N. Demirdoven, M. Khalil, A. Tokmakoff, J. Chem. Phys. 113 (2000) 9893.
[24] D.A. Blank, L.J. Kaufman, G.R. Fleming, J. Chem. Phys. 113 (2000) 771.
[25] D. McMorrow, W.T. Lotshaw, Chem. Phys. Lett. 174 (1990) 85.
[26] M.T. Asaki, C. Huang, D. Garvey, J. Zhou, H. Kapteyn, M. Murnane, Opt. Lett. 18 (1993) 977.
[27] T. Joo, Y.W. Jia, G.R. Fleming, Opt. Lett. 20 (1995) 389.
[28] J.C. Kirkwood, D.J. Ulness, A.C. Albrecht, M.J. Stimson, Chem. Phys. Lett. 293 (1998) 417.
[29] D. McMorrow, Opt. Commun. 86 (1990) 236.
[30] D. McMorrow, W.T. Lotshaw, G.A. Kenney-Wallace, IEEE Quant. Electron. 24 (1988) 441.
[31] D. McMorrow, W.T. Lotshaw, J. Phys. Chem. 95 (1991) 10395.
[32] W.T. Lotshaw, D. McMorrow, N. Thantu, J.S. Melinger, R. Kitchenham, J. Raman Spectrosc. 26 (1995) 571.
[33] D. McMorrow, N. Thantu, J.S. Melinger, S.K. Kim, W.T. Lotshaw, J. Phys. Chem. 100 (1996) 10389.
[34] M. Cho, M. Du, N.F. Scherer, G.R. Fleming, S. Mukamel, J. Chem. Phys. 99 (1993) 2410.
[35] L.D. Ziegler, R. Fan, A.E. Desrosiers, N.F. Scherer, J. Chem. Phys. 100 (1994) 1823.
[36] P. Cong, J.D. Simon, C.Y. She, J. Chem. Phys. 104 (1995) 962.
[37] M. Khalil, O. Golonzka, N. Demirdoven, C.J. Fecko, A. Tokmakoff, Chem. Phys. Lett. 321 (2000) 231.
[38] G.D. Goodno, R.J.D. Miller, J. Phys. Chem. A 103 (1999) 10619.
[39] M. Khalil, N. Demirdoven, O. Golonzka, C.J. Fecko, A. Tokmakoff, J. Phys. Chem. A 104 (2000) 5711.
[40] S. Mukamel, Principles of Nonlinear Optical Spectroscopy, first ed., Oxford University Press, New York, 1995.
[41] A.E. Siegman, Lasers, University Science Books, Mill Valley, 1986.
[42] J.A. Gardecki, G. Yu, S. Constantine, J. Peng, Y. Zhou, L.D. Ziegler, J. Chem. Phys. 114 (2001) 3586.
[43] L.J. Kaufman, D.A. Blank, G.R. Fleming, unpublished results, 1999.
[44] A.G. Marshall, F.R. Verdun, Fourier Transforms in NMR, Optical, Mass Spectrometry, Elsevier, New York, 1990.